Gram-level synthesis of core–shell structured catalysts for the oxygen reduction reaction in proton exchange membrane fuel cells

CrossMark

Mingchuan Luo, Lingli Wei, Fanghui Wang, Kefei Han, Hong Zhu[*]

State Key Laboratory of Chemical Resource Engineering, Institute of Modern Catalysis, Department of Organic Chemistry, School of Science, Beijing University of Chemical Technology, Beijing 100029, China

HIGHLIGHTS

- A facile route base on microwave-assisted polyol process and chemical dealloying process is proposed.
- Gram-level core–shell structured catalysts (Cu@Pt/C) for ORR are produced in one pot.
- Both spherical and cubooctahedral CuPt alloy nanocrystals are obtained in this system.
- The Cu@Pt/C catalyst shows higher electrocatalytic activity over CuPt/C and commercial Pt/C catalysts.

GRAPHICAL ABSTRACT
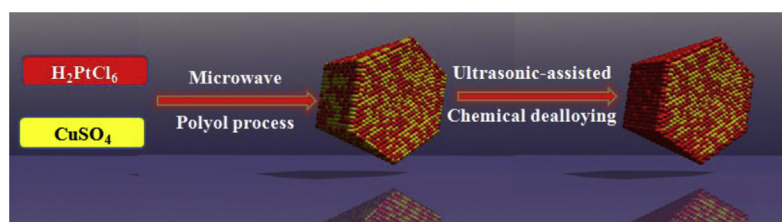
ARTICLE INFO

ABSTRACT

Over the past decade, Pt based core–shell structured alloys have been studied extensively as oxygen reduction reaction (ORR) catalysts for proton exchange membrane fuel cells (PEMFCs) because of their distinctive electrochemical performance and low Pt loading. In this paper, a facile route based on microwave-assisted polyol method and chemical dealloying process is proposed to synthesize carbon supported core–shell structured nanoparticles (NPs) in gram-level for ORR electrocatalysis in PEMFCs. The obtained samples are characterized by X-ray diffraction (XRD), transmission electron microscopy (TEM), energy dispersive X-ray spectroscopy (EDX), inductively coupled plasma atomic emission spectroscopy (ICP-AES), and X-ray photoelectron spectroscopy (XPS). These physical characterization indicate that the final synthesized NPs are highly dispersed on the carbon support, and in a core–shell structure with CuPt alloy as the core and Pt as the shell. Electrochemical measurements, conducted by cyclic voltammetry (CV) and rotating disk electrode (RDE) tests, show the core–shell structured catalyst exhibit a 3× increase in mass activity and a 2× increase in specific activity over the commercial Pt/C catalyst, respectively. These results demonstrate that this route can be a reliable way to synthesize low-Pt catalyst in large-scale for PEMFCs.

1. Introduction

It is imperative for the world to commit to clean energy innovation [1]. Proton exchange membrane fuel cells (PEMFCs) have been recognized as one of the most promising energy converting devices because of their low environmental impact, high power density, and high efficiency in energy conversion [2–5]. PEMFCs generate electricity by an electrochemical reaction in which oxygen and a hydrogen-rich fuel combine to generate water. Both the anodic fuel oxidation reaction and the cathodic oxygen reduction reaction (ORR) need a catalyst to lower their electrochemical overpotentials and to obtain high power output, and platinum

* Corresponding author. Fax: +86 10 64444919.
  E-mail address: zhuho128@126.com (H. Zhu).

nanoparticles (NPs) supported on carbon black have been used in current fuel cell prototypes. However, Pt is an expensive and scarce metal; the cost of Pt catalysts accounts for about 50% of the total cost of the fuel cell stack, especially at the cathode where ORR happens. Therefore, development of highly active and low-Pt loading ORR catalysts is a major challenge that concerns the commercialization of PEMFCs [6,7].

Making Pt-based alloy into a core–shell structure is a promising strategy to lower Pt loading and to increase activity. In this structure, several atomic lays of Pt or Pt alloy are deposited on another cheaper metal core, so that Pt usage is greatly reduced. Besides, the activity and durability of the Pt shell can be also enhanced by the structure-induced strain effect and ligand effect [8–12]. The field of electrocatalysis on core–shell structured NPs has seen many advances over the past two decades. Stamenkovic and co-workers prepared a Pt-skin surface on cheaper transition metal core by annealing-induced segregation in Pt-transition metal alloys [8,13,14]. The Pt-skin surface is 10-fold more active for the ORR than the corresponding Pt (111) surface and 90-fold more active than the state-of-the-art Pt/C catalysts for PEMFCs. Adzic and co-workers proposed a route which includes under-potential deposition and galvanic replacement to prepare monolayer platinum core–shell structured catalyst [15–17]. Theoretically, this monolayer core–shell structure could make full use of precious metal Pt, and the mass activity was reported to exceed the U.S. Department of Energy's 2017 technical targets (0.44 A mg^{-1} Pt @ 900 mV$_{iR-free}$) for large-scale automotive applications [18]. Strasser and co-workers synthesized a series of core–shell catalysts by electrochemical dealloying method [11,19–21]. Their dealloyed catalysts generally showed a surface catalytic improvement of a factor up to 4 in terms of Pt mass activity and of more than 10 in terms of specific activity compared to the commercial Pt/C catalysts. The core–shell structure induced lattice strain was regarded to play the most important role in enhancing the activity. Seed-mediated growth method is another widely used method to prepare core–shell structured NPs [22–24]. A famous example is the synthesis of PdPt nanodendrites (NDs) reported by Xia's group [25]. The PdPt NDs were 2.5× more active for the ORR over the commercial Pt/C catalyst based on Pt mass. They concluded that the observed high activity for PdPt NDs results from the high area intrinsic to the dendritic morphology and the exposure of particularly active facets toward the ORR on the Pt branches.

Although core–shell structured catalysts have been proven to be one of the best solutions to enhance activity and lower the Pt loading, there are limited reports on the large-scale produce of NPs in core–shell structure due to complicated synthesis procedure. In this study, a facile route without long heating time, long-chain surfactant agent and electrochemical equipment was developed to synthesize gram-level carbon black supported Cu–Pt core–shell structured catalysts (Cu@Pt/C) for the ORR in laboratory. More specifically, this route conducted in one pot includes a microwave assisted polyol process and a chemical surface dealloying process. X-ray diffraction (XRD), transmission electron microscopy (TEM), Energy dispersive X-ray spectroscopy (EDX), inductively coupled plasma atomic emission spectroscopy (ICP-AES), X-ray photoelectron spectroscopy (XPS), and rotating disk electrode (RDE) tests have been used to examine the physical structure and electrochemical performance of the synthesized Cu@Pt/C catalyst.

2. Experimental

2.1. Materials

Hexachloroplatinic acid (H$_2$PtCl$_6$·6H$_2$O), copper sulfate (CuSO$_4$·5H$_2$O), potassium hydroxide (KOH) and ethylene glycol (EG) were of analytical grade from the Beijing Chemical Factory of China. 5 wt% Nafion solutions were purchased from Dupont. Commercial carbon supported platinum catalyst (40 wt%, denoted as JM Pt/C) were purchased from Johnson Matthey. All chemicals above were used as received. Carbon black (Vulcan XC-72R) was obtained from Cabot Corp., and it was functionalized by a conventional acid treatment prior to using.

2.2. Catalysts preparation

Carbon black supported Cu$_x$Pt$_y$ alloy catalysts (Cu$_x$Pt$_y$/C) with nominal metal loading of 40 wt% were synthesized by a microwave-assisted polyol process. The bulk compositions of the alloy samples were controlled by adjusting the initial Pt and Cu precursor ratios. In brief, for Cu$_1$Pt$_1$/C catalyst, 600 mg functionalized carbon black was dispersed into 340 mL ethylene glycol (EG) and sonicated for 30 min. Then, 40 mL H$_2$PtCl$_6$·6H$_2$O/EG solution (20 g L^{-1}) and 97.3 mL CuSO$_4$·5H$_2$O/EG (4 g L^{-1}) were added to the mixture under magnetic stirring. After stirring for another 30 min, the pH of the above system was adjusted to 10 by the dropwise addition of 1 mol L^{-1} KOH/EG solution under vigorous stirring (the initial pH value was about 0.8). The resulting suspension was then placed into a flask and heated by a microwave reactor (Apex, China). The power of microwave, reactive temperature and time were 600 W, 170 °C and 8 min respectively. After heating, the solution was allowed to cool down to room temperature. For chemical dealloying process, 1 M HNO$_3$ solution was then added to the cooled mixture to preferentially remove Cu atoms from the surface of the precursor CuPt alloy NPs in an ultrasound cleaner, and the solution pH was adjusted to 1. The mixture was kept stirring for 2 h followed by filtered and washed with ethanol and water. The resulting catalyst was freeze-dried overnight, collected and weighed. A mortar was employed to homogeneously grind the material to form a fine powder. The obtained black samples were denoted as CuPt/C (without the adding of HNO$_3$) and Cu@Pt/C (with the adding of HNO$_3$), respectively.

2.3. Physical characterization

The catalysts were characterized by X-ray diffraction (XRD) on a Shimadzu XD-3A diffractometer (Japan) using a filtered Cu Ka radiation and operated at 35 kV at room temperature and a scanning rate of 4°/min. The (220) peak around $2\theta = 70°$ was selected to estimate the particle size by using Scherrer's equation and the lattice parameters were obtained by refining the unit cell dimensions by the least-squares method. The morphologies of the prepared catalysts were observed by using a transmission electron microscope (JEOL JEM-3010HR, Japan). The average chemical composition of the catalysts was determined by using an inductively coupled plasma atomic emission spectroscopy (ICP-AES) system (Agilent Technologies, USA) and energy-dispersive X-ray spectroscopy (EDX) detector. Thermo-gravimetric analysis (TGA) was further carried out to estimate the metal loading of the carbon support. The near-surface composition of the catalysts powder was measured by using an X-ray photoelectron spectrometer (XPS, LAB250 ESCA System, Thermo Fisher, USA) with an Al Ka radiation source. The XPS spectra were fitted by using the XPS Peak 4.1 software, in which a Shirley background was used to perform curve fitting and to calculate the atomic concentrations.

2.4. Electrochemical measurements

The electrochemical experiments were performed at room temperature by using thin film RDE method with Zennium electrochemical work station (Zahner, Germany). A conventional three-electrode cell was used in cyclic voltammetry (CV) and linear

sweep voltammetry (LSV). A platinum wire was used as the counter electrode; a saturated calomel electrode (SCE), separated by an electrolytic bridge from the main cell compartment was used as the reference electrode; however, all reported potentials are given with respect to the reversible hydrogen electrode (RHE). A polished glassy carbon electrode (5 mm in diameter) covered with a thin layer of catalysts was used as the working electrode. In detail, the glassy carbon electrode was polished using a 0.05 μm Al_2O_3 slurry and washed ultrasonically with ethanol and water separately for cleaning process. A stock solution of 20% isopropanol and 0.02% Nafion ionomer was prepared by mixing 5 mL of isopropanol with 19.9 mL of ultrapure water and 0.1 mL of 5 wt% Nafion ionomer solution (DuPont) in a 25 mL volumetric flask. Next, 2 mg of the catalyst was measured into a 5 mL vial and 2 mL of the above solution was added; The catalyst ink was then transferred to an ultrasonicator and sonicated for 30 min in a water bath with temperature less than 40 °C. 10 μL of the homogeneous catalyst ink was then drop-casted onto a clean glassy carbon electrode and dried at room temperature, yielding a loading of about 20 μg_{meta} cm^{-2} for all samples. The CV tests were conducted at 50 mV s^{-1} in a solution of N_2-saturated 0.1 mol L^{-1} $HClO_4$, and the potential range is 0.05–1.1 V. Prior to measuring the CVs for electrochemical surface area determination and the ORR, the prepared working electrode was electrochemically cleaned and stabilized by cycling between 0.05 and 1.1 V for 10 cycles at 200 mV s^{-1}. The LSV measurements were conducted with a rotating disk electrode (RDE) setup with rotating control (Pine Instruments) in O_2-saturated 0.1 mol L^{-1} $HClO_4$ from 0.05 to 1.1 V at a scan rate of 10 mV s^{-1} and rotational rate of 1600 rpm.

3. Results and discussion

3.1. Synthesis route of Cu$_x$@Pt$_y$/C catalysts

A schematic of the synthesis of Cu$_x$@Pt$_y$/C catalysts is shown in Fig. 1. Firstly, Cu$_x$Pt$_y$ alloy NPs were synthesized by a microwave-assisted polyol process with EG as solvent and reducing agent. This EG method has been wildly used in the synthesis of monometallic and bimetallic NPs because of its convenience, high quality and low cost [26–29]. Generally, the synthesis is carried out by heating at 100–150 °C in an oil bath for several hours in order to decompose EG into aldehyde as the reducing agent and then into glycolate as the stabilizer [30]. As the solvent is heated by conduction and convection in the oil-bath heating, there is a large temperature distribution within the solvent, especially in large-scale synthesis. The temperature distribution would then leads to poly-dispersed and aggregated NPs due to inhomogeneous nucleating. In contrast to oil-bath heating, the microwave dielectric heating can provide rapid and uniform heating for the whole reactive system, leading to uniform distribution with small sizes for NPs [31–33]. Moreover, the extremely high heating rate is benefit for the co-reduction of various metals with different reduction potential. This will be discussed further in Section 3.2.

Fig. 2. Filtered solution of polyol process (right) without the adding of HNO_3 and (left) with the adding of HNO_3.

In regard of surface dealloying process, electrochemical method was widely studied. In a typical electrochemical dealloying experiment, the Pt-based alloy catalysts were deposited on a glassy carbon electrode or the cathode of a membrane electrode assembly (MEA). Then the cathode potential was cycled at a given sweep rate and potential range for hundreds of times. Although this electrochemical dealloying method ensures the researchers to in-situ monitor and precisely control the surface dealloying reaction, only milligram (for MEA) or microgram (for glassy carbon electrode) level dealloyed products can be obtained because of the limited electrode areas. In contrast to electrochemical method, chemical dealloying is much easier to operate; meanwhile, it is more likely to be used for large-scale production. We conducted the chemical dealloying process in the same reactive pot because of the following two reasons: (1) Conducting in one pot costs less time and materials than conducting in a separate pot. (2) The yield of the whole reaction is enhanced. According to Kim and co-workers' research [29], the surface charge of carbon support depends on the pH value of the solution, and the zeta potential of the carbon support becomes more positive by changing the pH from alkaline to acid. In our experiment, the Pt alloy NPs, already negatively stabilized by glycolate anion, were attracted by the positively charged carbon surface in acidic solution. This was experimentally proven by a comparison of the filtered solution from the polyol process in alkaline and acid solution. As shown in Fig. 2, the color of filtered solution changes from brown (in web version) to transparency after the adding of HNO_3. This phenomenon suggests the suspended alloy colloidal NPs have loaded on the surface of carbon black after the pH adjustment step. This was also confirmed by TGA (Supporting information, Fig. S1, Table S1), which showed that the metal loading of Cu$_x$@Pt$_y$/C was higher than that of Cu$_x$Pt$_y$/C.

3.2. Physical characterization

As the MPt$_3$ (M represents 3d transition metal) alloy catalysts was studied most widely for ORR, the properties of CuPt$_3$/C catalyst
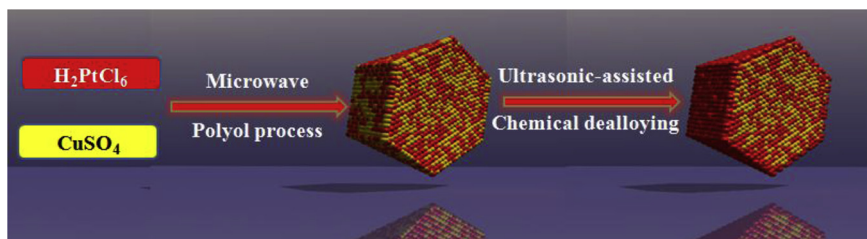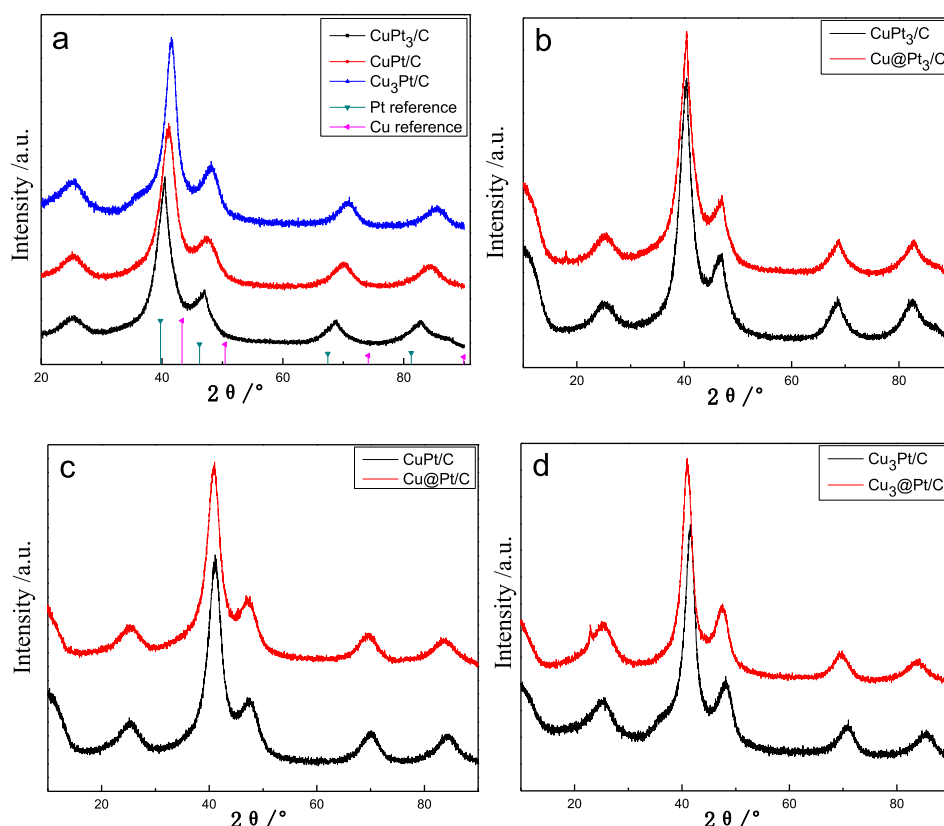

Fig. 1. Schematic of synthesis procedure of Cu$_x$@Pt$_y$/C catalysts.

Fig. 3. XRD patterns of (a) CuPt$_3$/C, CuPt/C and Cu$_3$Pt/C; (b) CuPt$_3$ and Cu@Pt$_3$; (c) CuPt and Cu@Pt; (d) Cu$_3$Pt and Cu$_3$@Pt catalysts. The standard diffraction peaks for Pt and Cu metals are also shown in (a) for comparison.

and its corresponding dealloyed catalyst would be mainly discussed in this study.

Fig. 3a shows representative powder XRD patterns of as-prepared Cu$_x$Pt$_y$/C catalysts with different Cu/Pt atomic ratios, the positions of diffraction peaks for pure Pt (70-2057, JCPDS-ICDD) and Cu (70-3038, JCPDS-ICDD) metals, respectively. The diffraction peak at 2θ value of 25°is attributed to the graphite (200) plane of the supporting carbon material. The diffraction pattern of Cu$_x$Pt$_y$ NPs could be readily indexed to (111), (200), (220) and (311) planes of face-centered cubic (fcc) lattice and located between those of the two pure metals, indicating the formations of Cu$_x$Pt$_y$ alloys [34]. Another evidence for the alloying of Cu and Pt is the absence of corresponding fcc peaks for pure Cu and Pt, otherwise the pure Cu or Pt NPs must be too small to be detected or in amorphous state. The fcc peak positions of alloys shift to higher angles with increasing Cu content, suggesting a lattice contraction which is caused by the incorporation of smaller Cu atoms into Pt fcc structure [35]. The lattice parameter of CuPt$_3$/C sample was refined to 3.856 Å and its composition is determined to be Cu$_{22}$Pt$_{78}$ from

Vegard's Law, which is very close to the nominal composition. The crystallite sizes as well as the lattice parameters of other synthesized catalysts were calculated using the XRD data, and the results are summarized in Table 1. From the above XRD analysis, we can conclude that this microwave-assisted polyol process is an effect way to synthesize Pt-based alloy NPs.

The XRD peaks of all dealloyed catalysts moved in the negative direction compared to respective alloys catalysts, indicative of the removal of surface Cu atoms, the expansion of the lattice constant and the maintenance of disordered fcc structure (Fig. 3b–d). However, the diffraction peaks of Cu$_x$@Pt$_y$ NPs still located between those of the two pure metals, and this may be a result of the lattice strain effect in the Pt shell that is known to modify the electronic structure of the metal through changes in orbital overlap [36]. Theoretically, a compressive-strain forms in Pt-enriched surface layers that are supported on a Cu$_x$Pt$_y$ alloy core with a smaller lattice parameter. Then, the formed compression weakens the adsorption energy of reactive intermediates via modifying the d-band structure of Pt atoms, and thereby enhances the catalytic activity [37,38].

Table 1
Comparison of compositions, particle size and lattice parameters determined from XRD, ICP, TEM and XPS.

| Samples	Cu:Pt ratio (EDX)	Cu:Pt ratio (ICP)	Near-surface Cu:Pt ratio (XPS)	Particle size (TEM)	Particle size (XRD)	Lattice parameters (XRD)
J-M Pt/C	0:100	0:100	0:100	3.31	3.20	3.921
Cu$_3$Pt/C	65:35	67:33	62:38	5.63	4.81	3.760
Cu$_3$@Pt/C	41:59	40:60	15:85	5.17	4.52	3.821
CuPt/C	43:57	45:55	40:60	4.15	4.10	3.802
Cu@Pt/C	29:71	32:68	11:89	4.11	4.01	3.855
CuPt$_3$/C	22:78	24:76	19:81	3.83	3.71	3.872
Cu@Pt$_3$/C	11:89	9:91	2:98	3.71	3.59	3.889
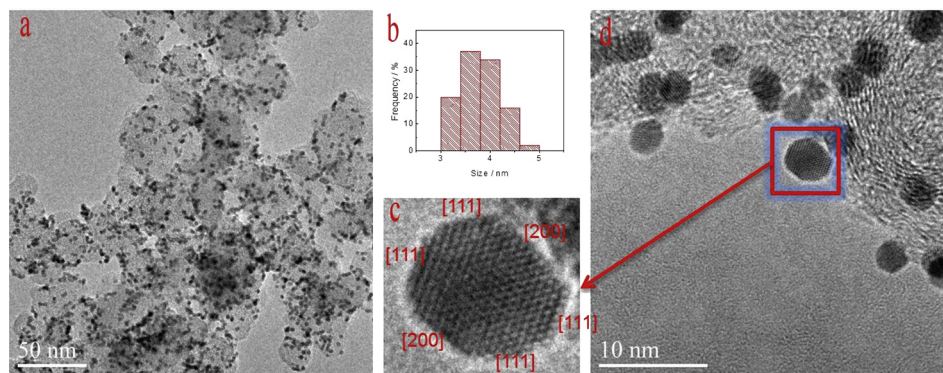
Fig. 4. Characterization of CuPt$_3$/C catalyst: (a) TEM image of CuPt$_3$/C catalyst; (b) histogram of particle size; (c) expanded view of an individual nanoparticle; (d) high-resolution TEM of CuPt$_3$/C catalyst.

A typical TEM image of as-prepared CuPt$_3$/C catalyst illustrates that the synthesized alloy NPs are highly dispersed on the carbon supports (Fig. 4a). Fig. 4b shows the particle size distribution histogram of CuPt$_3$/C catalyst based on the statistics of 300 NPs. The average particle size determined to be 3.83 nm is in a narrow size range and identical with the result of XRD (Table 1). The sizes of these alloy NPs are in the optimal range for fuel cells catalysts [39]. As shown in Fig. 5, the average size of alloy NPs decreases slightly to 3.71 nm after chemical dealloying process as a result of the removal of surface Cu atoms. The high resolution TEM image of CuPt$_3$/C was shown in Fig. 4d. It was found that the visible one-dimensional lattice fringes correspond to a spacing of 0.22 nm, which matches well with the expected *d* spacing of the (111) plane of CuPt$_3$ alloy. Most of the alloy NPs are spherical as a result of two effects: (i) the inclination of NPs from the low index zone axis make the faceted corners appear to be slightly curved; (ii) the interference from the carbon substrate that obscures sharp edges and corners [40,41]. However, alloy NPs with size larger than 5 nm tended to show cubooctahedral shapes in this work, and a typical cubooctahedral CuPt$_3$ NP is shown in Fig. 4c. This phenomenon indicates that microwave assisted polyol method may be a potential way to synthesize alloy NPs with desired faceted shapes.

Fig. 6 shows the EDX spectra of as-prepared CuPt$_3$/C and Cu@Pt$_3$/C catalysts as well as the corresponding elemental mapping of Cu and Pt. The elemental mapping analysis demonstrates that both metals distributed on carbon black very uniformly, and the amount of Cu decreased sharply after chemical dealloying process. Quantitative results determined by EDX show that the metal

compositions of CuPt$_3$/C and Cu@Pt$_3$ catalysts are Cu$_{22}$Pt$_{78}$ and Cu$_{11}$Pt$_{89}$, respectively. The compositions were further checked by ICP analyses, which is identical with the EDX results (Table 1). These results are similar to the compositions change after electrochemical dealloying reported by Strasser's group [19], suggesting both chemical and electrochemical method can obtain core–shell structure NPs with thermodynamic stability. The pure Pt skeleton formed after dealloying was deemed to protect the subsurface transition metal atoms from further dissolution. However, Cui and co-workers found that the atomic fraction of Cu further decreased with the protection of Pt layers if the electrochemical dealloying process continued between 0.05 and 1.2 V. They gave the possible reason that the Cu atoms in the core region migrate to the surface by surface segregation effect [42].

Fig. 7 shows the XPS survey spectra of CuPt$_3$/C and Cu@Pt$_3$/C catalysts. From the XPS spectra, we can see that the characteristic peaks of Cu decrease dramatically after the chemical dealloying process while the characteristic peaks of Pt witness little change. This comparison provides compelling evidence that most of Cu atoms were removed from the surfaces of NPs. As shown in Table 1,
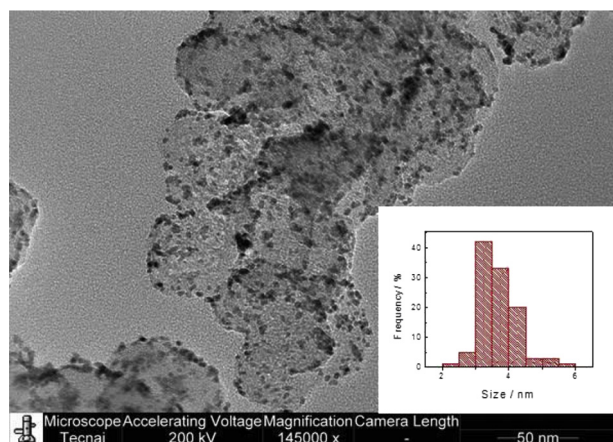
Fig. 5. TEM image of Cu@Pt$_3$/C catalyst and corresponding histogram of particle size.
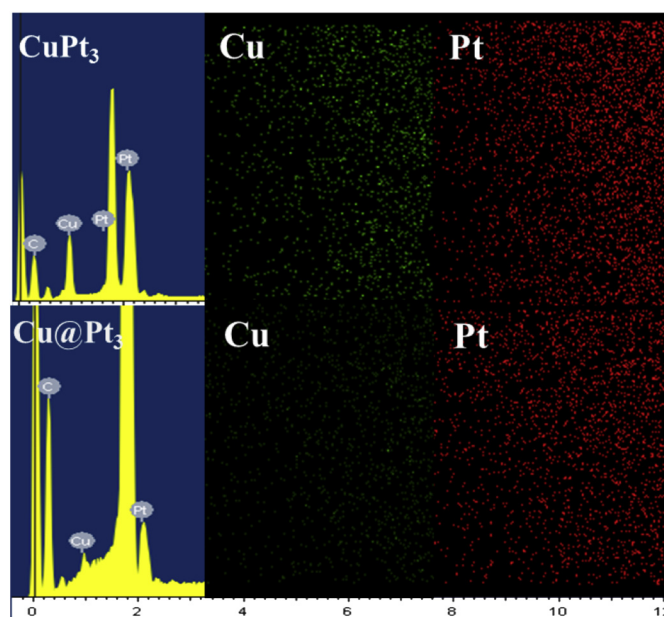
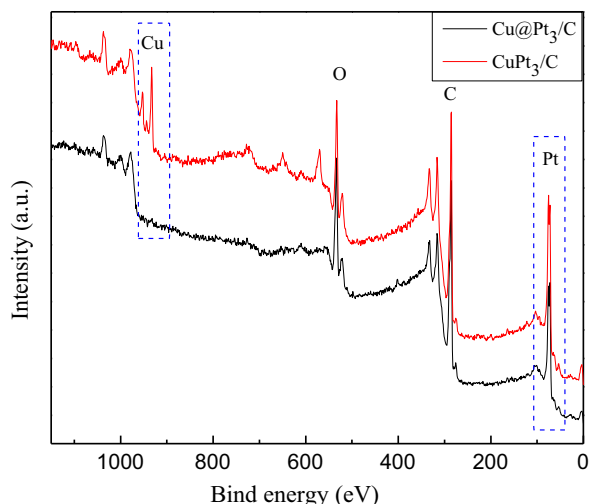**Fig. 6.** EDX spectra of CuPt$_3$/C and Cu@Pt$_3$/C catalysts, and the corresponding elemental mapping of Cu and Pt.

Fig. 7. XPS survey spectra of CuPt$_3$/C and Cu@Pt$_3$/C catalysts.
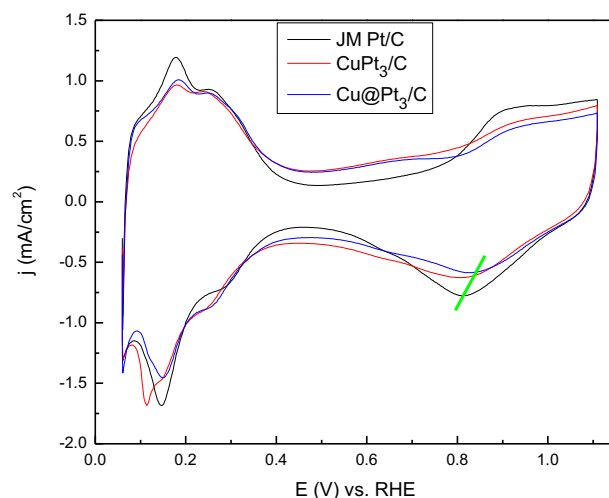

Fig. 8. CV curves of JM Pt/C, CuPt$_3$/C and Cu@Pt$_3$/C catalysts measured in N$_2$-purged 0.1 mol L^{-1} HClO$_4$ at room temperature. Sweep rate: 50 mV s^{-1}.

the composition ratio between Cu and Pt in the surface region for CuPt$_3$/C and Cu@Pt$_3$/C are Cu$_{19}$Pt$_{81}$ and Cu$_2$Pt$_{98}$, respectively. The near-surface compositions of dealloyed catalysts measured by XPS are quite different from those of total compositions determined by ICP and EDX. In general, the molar ratio of Cu/Pt in near-surface region is much smaller than that in the whole particle, indicating that the dealloyed NPs are core–shell structured with a Cu$_x$Pt$_y$ alloy core and a pure Pt shell.

3.3. Electrochemical measurements

Fig. 8 shows the voltammetry curves for the JM Pt/C, CuPt$_3$/C and Cu@Pt$_3$/C catalysts after surface cleaning cycling. They all depict well-developed, underpotentially-deposited hydrogen adsorption/desorption region between 0.05 and 0.4 V as well as Pt–OH formation and reduction region between 0.7 and 1.0 V, suggesting an almost pure Pt catalyst surface. In the case of CuPt$_3$/C catalyst, however, a weak anodic current peak was observed at around 0.65 V on the first cleaning cycling (not shown here) and dropped rapidly in intensity during the second cycle. This weak anodic current peak represents slight Cu dissolution from the synthesized CuPt$_3$ alloy surface. No Cu dissolution peak was observable for Cu@Pt$_3$/C catalyst, indicative of complete removal of surface Cu in chemical dealloying process. The electrochemical surface area (ESA) was determined by integrating the hydrogen desorption area in the potential range 0.075–0.4 V after subtracting the double-layer capacitance and applying a charge density of 0.21 mC cm^{-2} for the charge required to oxidize a monolayer of hydrogen on Pt surface. The ESA of a catalyst in terms of platinum is calculated according to the following equation:

$$ESA_{Pt}\left(m^2\,g^{-1}\right) = \left[\frac{Q_H(mC)}{0.21\left(mC\,cm^{-2}\right) \times L_{Pt}\left(mg\,cm^{-2}\right) \times A_g\left(cm^2\right)}\right] \times 10$$

(1)

where Q_H (mC) is the charge exchanged during hydrogen adsorption on Pt surface, and L_{Pt} (mg cm^{-2}) is the working electrode's Pt loading and A_g (cm^2) is the geometric surface area of the glassy carbon electrode (i.e., 0.196 cm^2). Based on Eq. (1), the values of ESA$_{Pt}$ (m^2 g^{-1}) for JM Pt/C, CuPt$_3$/C and Cu@Pt$_3$/C are 53.52 m^2 g^{-1}, 54.33 m^2 g^{-1} and 62.86 m^2 g^{-1}, respectively. Considering that the

particle size of Pt/C is smaller than that of Cu@Pt$_3$/C, an increase in Pt utilization was achieved in our core-sell structured catalyst.

It is generally believed that the specific activity of Pt-based catalysts can be enhanced by delaying the intermediate oxide (such as OH, OOH) adsorbing. Careful inspection of cyclic voltammograms in Fig. 8 reveals that the oxide reduction peak obtained in the cathodic sweep for the Cu@Pt$_3$/C catalyst occurs ca. 80 mV positive compared to that on the JM Pt/C catalyst, while that on the CuPt$_3$/C catalyst falls in between. In agreement with the oxide desorption wave, the onset potential of oxide adsorption obtained in the anodic sweep for the CuPt$_3$/C catalyst lies between that for Cu@Pt$_3$/C and Pt/C catalysts, indicating that the fractional coverage by oxide increase in the order: Cu@Pt$_3$/C < CuPt$_3$/C < Pt/C, which also means that the Cu@Pt$_3$/C catalyst provides more reaction sites than the other two catalysts and thus shows the highest activity [8].

The activities of as-prepared catalysts were measured using an RDE operated at 1600 rpm in O$_2$-saturated 0.1 mol L^{-1} HClO$_4$ at a scan rate of 10 mV s^{-1}. The polarization curves of CuPt$_3$/C and Cu@Pt$_3$/C catalysts are shown in Fig. 9a and the curve of JM Pt/C catalyst is also shown in this figure for comparison. The limiting current density plateau is well developed for all three catalysts. The electrocatalytic activities of the catalysts, as estimated from the half-wave potentials ($E_{1/2}$), were maximized for Cu@Pt$_3$/C. In detail, the $E_{1/2}$ of Cu@Pt$_3$/C is 0.89 V, approximate 50 mV higher than that of the JM Pt/C and 30 mV higher than that of CuPt$_3$/C. In order to establish the internal structure–function relationship, the kinetic current associated with the intrinsic activity of each catalyst was obtained using the Koutechy–Levich equation:

$$I_k = (I_{lim} \times I)/(I_{lim} - I)$$

(2)

where I_k is the kinetic current (A) and I_{lim} is the measured limited current (A). First, the ORR polarization curves are corrected by subtracting background current measured under identical conditions in N$_2$ atmosphere without rotation. Then, I is the value of the curve at $E = 0.90$ V and I_{lim} is that at $E = 0.40$ V versus RHE. The Pt mass activities and specific activities are estimated via calculation of I_k and normalization to the Pt loading of the disk electrode and to the Pt electrochemical surface area, respectively. The Pt mass activity at 0.9 V was 0.23 A mg^{-1}$_{Pt}$ for Cu@Pt$_3$/C, over 3 folds higher than that for Pt/C (0.07 A mg^{-1}$_{Pt}$, Fig. 9b). Meanwhile, the specific activity reached 0.36 mA cm^{-2} for Cu@Pt$_3$/C and 0.23 for CuPt$_3$/C,
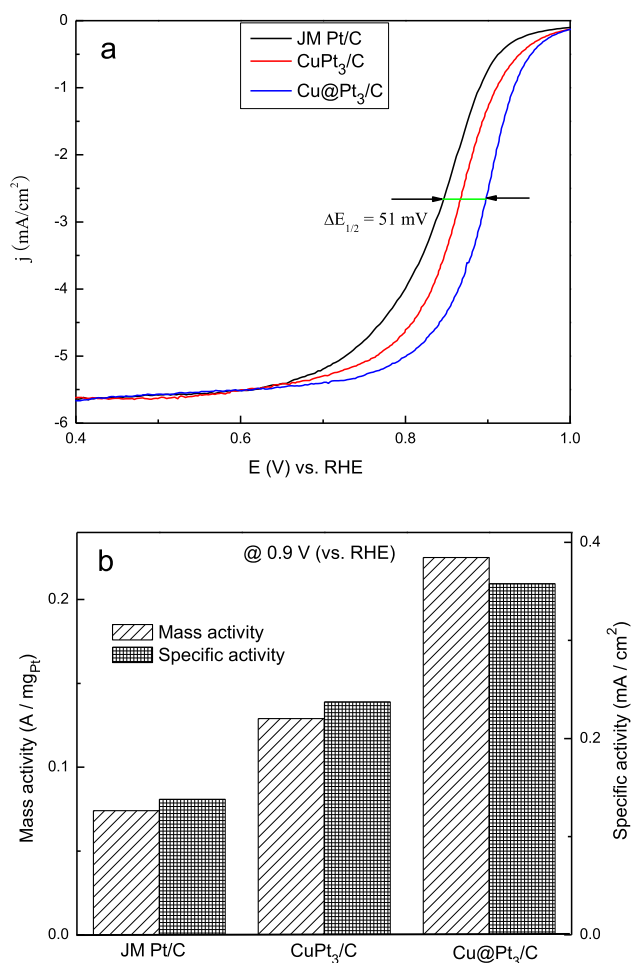
Fig. 9. (a) Polarization curves and (b) mass and specific activities of JM Pt/C, CuPt$_3$/C and Cu@Pt$_3$/C catalysts in O$_2$-saturated 0.1 mol L^{-1} HClO$_4$ at a rotation rate of 1600 rpm. Sweep rate: 10 mV s^{-1}.

indicating that the intrinsic ORR activity of the prepared core–shell structure catalyst was over 2 times that of the JM Pt/C catalyst.

The enhanced ORR activity of Cu@Pt$_3$/C catalyst over the commercial Pt/C catalyst in this study can be attributed to two core-–shell structure induced effects: i (ligand effect) Alloying of Pt with Cu increased the Pt *d*-band vacancy [43]; ii (geometric effect) Strain formed in the Pt shells that are supported on CuPt alloy core with a smaller lattice parameter [11]. The co-existence of ligand and geometric effects modify the *d*-band structure of the surface Pt atoms on the core–shell structured NPs, and thereby weakened the adsorption energy of reactive intermediates compared to pure Pt crystallite surface and led to an increase in the ORR catalytic reactivity.

4. Conclusions

In summary, we reported a synthesis route which could be applied in large-scale production of Pt-based core–shell structured catalyst for oxygen reduction reaction in PEMFCs. This synthesis route was based on microwave-assisted polyol process and chemical dealloying process. XRD and TEM tests showed that spherical and cuboctahedral nanocrystals surrounded by (111) and (200) planes were obtained in this system. Compositional results confirmed Cu was selectively removed from the surface of alloy NPs, resulting in a core–shell structure with CuPt alloy as the core and Pt as the shell. The electrochemical activity of core–shell

structured catalyst towards ORR was much higher than that of commercial Pt/C catalyst. The combined impact of enlarged ESA, ligand effect and geometric effect was responsible for the enhanced electrochemical performance of Cu@Pt/C catalyst synthesized by this route.

Appendix A. Supplementary data

Supplementary data related to this article can be found at http://dx.doi.org/10.1016/j.jpowsour.2014.07.102.

References

[1] B. Gates, Science 334 (2011) 877.
[2] H.A. Gasteiger, N.M. Markovic, Science 324 (2009) 48–49.
[3] M.K. Debe, Nature 486 (2012) 43–51.
[4] H.A. Gasteiger, S.S. Kocha, B. Sompalli, F.T. Wagner, Appl. Catal. B: Environ. 56 (2005) 9–35.
[5] C.W.B. Bezerra, L. Zhang, H. Liu, K. Lee, A.L.B. Marques, E.P. Marques, H. Wang, J. Zhang, J. Power Sources 173 (2007) 891–908.
[6] S. Guo, S. Zhang, S. Sun, Angew. Chem. Int. Ed. Engl. 52 (2013) 8526–8544.
[7] V. Mazumder, Y. Lee, S. Sun, Adv. Funct. Mater. 20 (2010) 1224–1231.
[8] V.R. Stamenkovic, B.S. Mun, M. Arenz, K.J. Mayrhofer, C.A. Lucas, G. Wang, P.N. Ross, N.M. Markovic, Nat. Mater. 6 (2007) 241–247.
[9] J. Snyder, I. McCue, K. Livi, J. Erlebacher, J. Am. Chem. Soc. 134 (2012) 8633–8645.
[10] D. Wang, H.L. Xin, R. Hovden, H. Wang, Y. Yu, D.A. Muller, F.J. DiSalvo, H.D. Abruña, Nat. Mater. 12 (2012) 81–87.
[11] P. Strasser, S. Koh, T. Anniyev, J. Greeley, K. More, C. Yu, Z. Liu, S. Kaya, D. Nordlund, H. Ogasawara, M.F. Toney, A. Nilsson, Nat. Chem. 2 (2010) 454–460.
[12] H. Yang, Angew. Chem. Int. Ed. Engl. 50 (2011) 2674–2676.
[13] V.R. Stamenkovic, B. Fowler, B.S. Mun, G. Wang, P.N. Ross, C.A. Lucas, N.M. Markovic, Science 315 (2007) 493–497.
[14] V.R. Stamenkovic, B.S. Mun, K.J. Mayrhofer, P.N. Ross, N.M. Markovic, J. Am. Chem. Soc. 128 (2006) 8813–8819.
[15] R.R. Adzic, J. Zhang, K. Sasaki, M.B. Vukmirovic, M. Shao, J.X. Wang, A.U. Nilekar, M. Mavrikakis, J.A. Valerio, F. Uribe, Top. Catal. 46 (2007) 249–262.
[16] J. Zhang, Y. Mo, M.B. Vukmirovic, R. Klie, K. Sasaki, R.R. Adzic, J. Phys. Chem. B 108 (2004) 10955–10964.
[17] J. Zhang, M.B. Vukmirovic, K. Sasaki, A.U. Nilekar, M. Mavrikakis, R.R. Adzic, J. Am. Chem. Soc. 127 (2005) 12480–12481.
[18] Multi-year research, development and demonstration plan: planned program activities for 2005–2015, U.S. Department of Energy, 2009.
[19] P. Mani, R. Srivastava, P. Strasser, J. Phys. Chem. C 112 (2008) 2770–2778.
[20] C. Cui, L. Gan, M. Heggen, S. Rudi, P. Strasser, Nat. Mater. 12 (2013) 765–771.
[21] L. Gan, M. Heggen, S. Rudi, P. Strasser, Nano Lett. 12 (2012) 5423–5430.
[22] C. Wang, D. van der Vliet, K.L. More, N.J. Zaluzec, S. Peng, S. Sun, H. Daimon, G. Wang, J. Greeley, J. Pearson, A.P. Paulikas, G. Karapetrov, D. Strmcnik, N.M. Markovic, V.R. Stamenkovic, Nano Lett. 11 (2011) 919–926.
[23] H. Zhu, M. Luo, S. Zhang, L. Wei, F. Wang, Z. Wang, Y. Wei, K. Han, Int. J. Hydrogen Energy 38 (2013) 3323–3329.
[24] J. Yang, X. Chen, X. Yang, J.Y. Ying, Energy & Environ. Sci. 5 (2012) 8976.
[25] B. Lim, M. Jiang, P.H. Camargo, E.C. Cho, J. Tao, X. Lu, Y. Zhu, Y. Xia, Science 324 (2009) 1302–1305.
[26] C. Bock, C. Paquet, M. Couillard, G.A. Botton, B.R. MacDougall, J. Am. Chem. Soc. 126 (2004) 8028–8037.
[27] R. Harpeness, A. Gedanken, Langmuir 20 (2004) 3431–3434.
[28] C. Grolleau, C. Coutanceau, F. Pierre, J.M. Leger, J. Power Sources 195 (2010) 1569–1576.
[29] H.-S. Oh, J.-G. Oh, H. Kim, J. Power Sources 183 (2008) 600–603.
[30] S. Harish, S. Baranton, C. Coutanceau, J. Joseph, J. Power Sources 214 (2012) 33–39.
[31] M. Tsuji, M. Hashimoto, Y. Nishizawa, M. Kubokawa, T. Tsuji, Chemistry 11 (2005) 440–452.
[32] E. Lebègue, S. Baranton, C. Coutanceau, J. Power Sources 196 (2011) 920–927.
[33] S.A. Galema, Chem. Soc. Rev. 26 (1997) 233.

[34] Z. Peng, H. You, H. Yang, Adv. Funct. Mater. 20 (2010) 3734–3741.
[35] D. Wang, H.L. Xin, H. Wang, Y. Yu, E. Rus, D.A. Muller, F.J. DiSalvo, H.D. Abruña, Chem. Mater. 24 (2012) 2274–2281.
[36] W. Yu, M.D. Porosoff, J.G. Chen, Chem. Rev. 112 (2012) 5780–5817.
[37] V. Jalan, J. Electrochem. Soc. 130 (1983) 2299.
[38] I. Dutta, M.K. Carpenter, M.P. Balogh, J.M. Ziegelbauer, T.E. Moylan, M.H. Atwan, N.P. Irish, J. Phys. Chem. C Nanomater. Interfaces 114 (2010) 16309–16320.
[39] K. Kinoshita, J. Electrochem. Soc. 137 (1990) 845–848.
[40] V. Radmilovic, H.A. Gasteiger, P.N. Ross, J. Catal. 154 (1995) 98–106.
[41] J.R.C. Salgado, E. Antolini, E.R. Gonzalez, J. Phys. Chem. B 108 (2004) 17767–17774.
[42] C. Cui, H. Li, X. Liu, M. Gao, S. Yu, ACS Catal. 2 (2012) 916–924.
[43] J. Greeley, I.E. Stephens, A.S. Bondarenko, T.P. Johansson, H.A. Hansen, T.F. Jaramillo, J. Rossmeisl, I. Chorkendorff, J.K. Norskov, Nat. Chem. 1 (2009) 552–556.